KeAi
CHINESE ROOTS
GLOBAL IMPACT

#### Contents lists available at ScienceDirect

## Petroleum Science

journal homepage: www.keaipublishing.com/en/journals/petroleum-science



## Original Paper

# Understanding the hydrocarbon-generation potential on jurassic coal-measure source rocks in the Junggar Basin: From the perspective of hydrogen-rich molecular structure



Tian-Chen Ge <sup>a</sup>, Xiang-Chun Chang <sup>a, b, \*</sup>, Guan-Long Zhang <sup>c</sup>, Jun-Jian Zhang <sup>a</sup>, Rui-Chao Guo <sup>c</sup>, Wei-Zheng Gao <sup>a</sup>, Ling-Yu Zhao <sup>a</sup>, Shang-Bin Wang <sup>a</sup>, Jia-Qi Duan <sup>d</sup>

- a College of Earth Science and Engineering, Shandong University of Science and Technology, Qingdao, 266590, Shandong, China
- <sup>b</sup> Laboratory for Marine Mineral Resources, Qingdao Marine Science and Technology Center, Qingdao, 266237, Shandong, China
- <sup>c</sup> Research Institute of Petroleum Exploration and Development, Shengli Oil Company, Sinopec, Dongying, 257001, Shandong, China
- <sup>d</sup> School of Geology and Mining Engineering, Xinjiang University, Urumqi, 830017, Xinjiang, China

#### ARTICLE INFO

# Article history: Received 6 November 2023 Received in revised form 30 January 2024 Accepted 13 March 2024 Available online 9 April 2024

Edited by Jie Hao and Meng-Jiao Zhou

Keywords: Coal-measure source rock Hydrocarbon potential Macromolecular structure Semi-open system pyrolysis Junggar basin

#### ABSTRACT

The Jurassic coal-measure source rocks in the Junggar Basin have drawn considerable attention in recent years. In our hydrocarbon thermal simulation experiments of these rocks, we found that the dark mudstone evaluated as good source rock, had a much lower hydrocarbon generation capacity than the coal and carbonaceous mudstone, evaluated as poor source rock. Based on this background, we performed Fourier transform infrared spectroscopy (FTIR) and combined the results of semi-open thermal simulation experiments to explore the association between the molecular structure and hydrocarbon production capacity, with the aim of obtaining a new understanding of hydrocarbon potential of Jurassic coal-measure source rocks from the perspective of molecular structure. The results indicate that coals exhibit lower condensation of aromatic structures and higher relative abundance of aliphatic structures with a higher degree of branched chaining than mudstones and carbonaceous mudstones. Apparent aromaticity  $(f_a)$ , aromatic abundance parameter I, and degree of condensation (DOC) are negatively correlated with organic matter abundance. The aliphatic structural parameter H demonstrates a substantial positive correlation with organic matter abundance. Furthermore, aliphatic relative abundance factor A is associated with the type of organic matter; the better is the type of the organic matter, the larger is the A value. The combination of the molecular structures with the thermal simulation results shows that the aliphatic hydrogen enrichment of selected carbonaceous mudstone is similar to that of coal. However, the relative abundance of the aliphatic group of it is high, and the DOC of the aromatic structure is low, making the hydrocarbon generation base stronger and easier to crack. Thus, the hydrocarbon generation capacity of carbonaceous mudstone is slightly higher than that of coal. Mudstone has low H and I values, and the DOC is high, indicating that its hydrocarbon base is low, so it has low hydrocarbon generation capacity. Therefore, the molecular structure is closely associated with the hydrocarbon potential of coal-measure source rocks. When evaluating the qualities of coal-measure source rocks, the influence of molecular structure on these rocks should be considered.

© 2024 The Authors. Publishing services by Elsevier B.V. on behalf of KeAi Communications Co. Ltd. This is an open access article under the CC BY license (http://creativecommons.org/licenses/by/4.0/).

#### 1. Introduction

The Jurassic in Junggar Basin is a typical coal-bearing formation that is composed of coals, carbonaceous mudstones, and dark

mudstones mainly distributed in the Badaowan ( $J_1b$ ), Sankonghe ( $J_1s$ ), and Xishanyao ( $J_2x$ ) formations (Cao et al., 2012; Gong et al., 2017; Gan et al., 2018; Yao et al., 2022; Wang et al., 2023). In recent years, large amounts of oil and gas produced by Jurassic source rocks have been discovered in the Piedmont depression belt of the southern basin, the Sikeshu Sag, and the Zhong 4 and Zhong 2 blocks of Sinopec (Zhang and Liu, 2002; Zeng, 2020; Hou et al., 2021a; Wu et al., 2020; Yu et al., 2022). Furthermore, the Jurassic coal-measure source rocks in the Junggar Basin have gained

<sup>\*</sup> Corresponding author. College of Earth Science and Engineering, Shandong University of Science and Technology, Qingdao, 266590, Shandong, China. E-mail address: xcchang@sina.com (X.-C. Chang).

increasing attention with the growing interest in the study of coalderived gas and oil. Numerous studies have been conducted on the organic matter abundance, type, and maturity of the Jurassic coalmeasure source rocks in different blocks, demonstrating features such as high total organic carbon content (TOC) values and macerals dominated by vitrinite, which is similar to the Tuha Basin coal strata (Li et al., 2009; Li et al., 2019; Qiao et al., 2020; Zeng, 2020). To guide future exploration, it is necessary to determine whether the Jurassic coal-measure source rocks have good hydrocarbon potential.

Many studies have investigated the hydrocarbon potential of coal-measure source rocks in the study area through hydrocarbon thermal simulation experiments but obtained contradictory results: Yang et al. (2021) concluded that the hydrocarbon potential of dark mudstones and coals are higher, whereas Yu et al. (2022) reported that carbonaceous mudstones have the highest hydrocarbon potential. Thus, which type of hydrocarbon source rock has more excellent hydrocarbon potential remains controversial. In our study, we found that the hydrocarbon-generating capacity of carbonaceous mudstones evaluated as fair source rocks was greater than that of mudstones evaluated as good source rocks. This suggests that the hydrocarbon potential of coal-measure source rocks is influenced by other factors. Previous studies have also demonstrated that some conventional parameters such as the H/C and HI are ineffective in evaluating the oil-generating potential of coal samples and terrestrial organic matter (Peters, 1986; Powell and Boreham, 1991; Curry et al., 1994; Isaksen et al., 1998; Killops et al., 1998). Therefore, determining how to scientifically evaluate the hydrocarbon potential of coal-measure source rocks is an issue that needs to be addressed.

The main hydrocarbon-generating macerals of coal-measure source rocks are exinite and matrix vitrinite (Peters, 1986; Killops et al., 1998). The Jurassic coal-measure source rocks in the Junggar Basin are similar to those in the Tuha Basin, with their microcomponents dominated by vitrinite, and their hydrocarbon potentials are linearly associated with the hydrogen-rich matrix vitrinite; this indicates that the hydrogen-rich structure is a critical influencing factor of the hydrocarbon potential of the coal-measure source rocks in the Junggar Basin (Tao et al., 2018; Wang et al., 2021; Zeng, 2020). In view of this, we conducted Fourier transform infrared spectroscopy (FTIR) experiments to explore the composition of the macromolecular structure of the coal-measure source rocks and demonstrate the association between the molecular structure and the hydrocarbon potential. In addition, we conducted semi-open thermal simulation experiments, attempted to demonstrate the phenomenon of the difference in the yield of various types of products that occurred in the thermal experiments through the molecular structure, and determined whether the organic macromolecular structure of the coal-measure source rocks can reflect the magnitude of their hydrocarbon generation potential.

### 2. Geological settings

The Junggar Basin is a closed triangular inland basin located in the eastern half of the Kazakhstan-Junggar Plate; it is bounded to the south by the Northern Tianshan and Bogda orogenic belts, to the west by the Junggar orogenic belt, and to the north by the Kramerian orogenic belt (Fig. 1(a)) (Zhi et al., 2023; Zhu et al., 2023a; Zhang and Wang, 2023).

The Jurassic coal-measure source rocks are widely distributed in the Junggar Basin, extending not only across the whole basin but also into the surrounding intermountain basins. These rocks are also mainly distributed in the Badaowan  $(J_1b)$ , Sangonghe  $(J_1s)$ , and Xishanyao  $(J_2x)$  formations. The lithology of the  $J_1b$  is essentially thick-bedded sandstone, sandy conglomerate interbedded with coal

seams, and dark mudstone; the lithology of the  $J_1s$  is mainly sandstone, sand conglomerate, and dark mudstone interbedded with thin coal seams; and the lithology of the  $J_2x$  is mainly dark gray mudstone and sandstone (Fig. 1(b)). Among them, the  $J_1b$  and  $J_2x$  have existed coal-gathering centers in both the southern and abdominal areas (Qiu et al., 2021; Zhang et al., 2022; Yang et al., 2022).

The Junggar Basin is a large superposition basin that has been formed by multiple phases of tectonic movements since the Paleozoic. In the early stage of the Paleozoic, the ancient ocean developed in the present western border mountain of the Junggar Basin, resulting in the separate formation of the Junggar-Turbo microplate. This microplate clashed and connected again with the Kazakhstan plate around the end of the Early Carboniferous period, generating the North Tianshan nappe structure and the Bogda tectonic belt (Li et al., 2016, 2018). From the Permian on, the seawater gradually withdrew to the southeast and transformed into a full-scale foreland basin, finally evolving into a large intraland depressional lake basin, with the Junggar Basin and adjacent areas all entering the era of intraland lake basins, of which the Early and Middle Permian belongs to the foreland basin stage, and the Late Permian and Triassic evolved into the intraland depressional stage (Zhu et al., 2023b). The Early and Middle Jurassic period is characterized by extensional subsidence, after which rightward twisting occurs, and gradually converts from extension to extrusion, and only the Changji Sag is characterized by continuous subsidence. After the Cretaceous, a large intraland unified depressional basin formed, the sedimentation center moved to the south. the thickness of the sediment increased, and the tectonic pattern of the southern depression and northern slope continued for a long time. During the Neoproterozoic and Quaternary, with the largescale uplift of the Northern Tianshan Mountains, the southern edge of the Junggar Basin strongly subsided, and a few alluvial folding zones developed (Long et al., 2023; Ding et al., 2020; Zeng, 2020; Zhu et al., 2023c).

### 3. Samples and experiments

#### 3.1. Samples

In this study, most of the samples were gathered from the Dongdaohaizi Sag, the Yongjin-Moxizhuang area in the middle of the basin, and the outcrops of the Tiechanggou (TCG) and Haojiagou (HJG) areas in the southern edge of the basin (Fig. 1(a)). The samples cover three major Jurassic formations (J1s, J1b, and J2x), including 10 dark mudstone samples (N1–N10), 6 carbonaceous mudstone samples (TN1–TN6), and 3 coal samples (M1–M3).

#### 3.2. TOC and rock-eval analysis

The TOC of the samples was measured using a LECO CS-230 analyzer, and the rock pyrolysis experiment was conducted using a Rock-Eval-VI instrument. This instrument was also used to measure S<sub>1</sub>, S<sub>2</sub>, and  $T_{\rm max}$  (temperature of maximum kerogen cracking) in accordance with the Chinese Petroleum Industry Standard of Rock-Eval analysis GB/T (18602-2012).

#### 3.3. Fourier transform infrared spectroscopy measurements

The instrument used in the FTIR measurements was a Vertex 80v infrared spectrometer (Bruker, Germany). The samples underwent KBr press pretreatment after being crushed to less than 200 mesh. For complete pulverization and mixing, 500 mg of KBr powder and 5 mg of coal sample were ground in an agate mortar for 10 min. Then,  $P_2O_5$  was used to dry the pellets under a vacuum for 48 h.

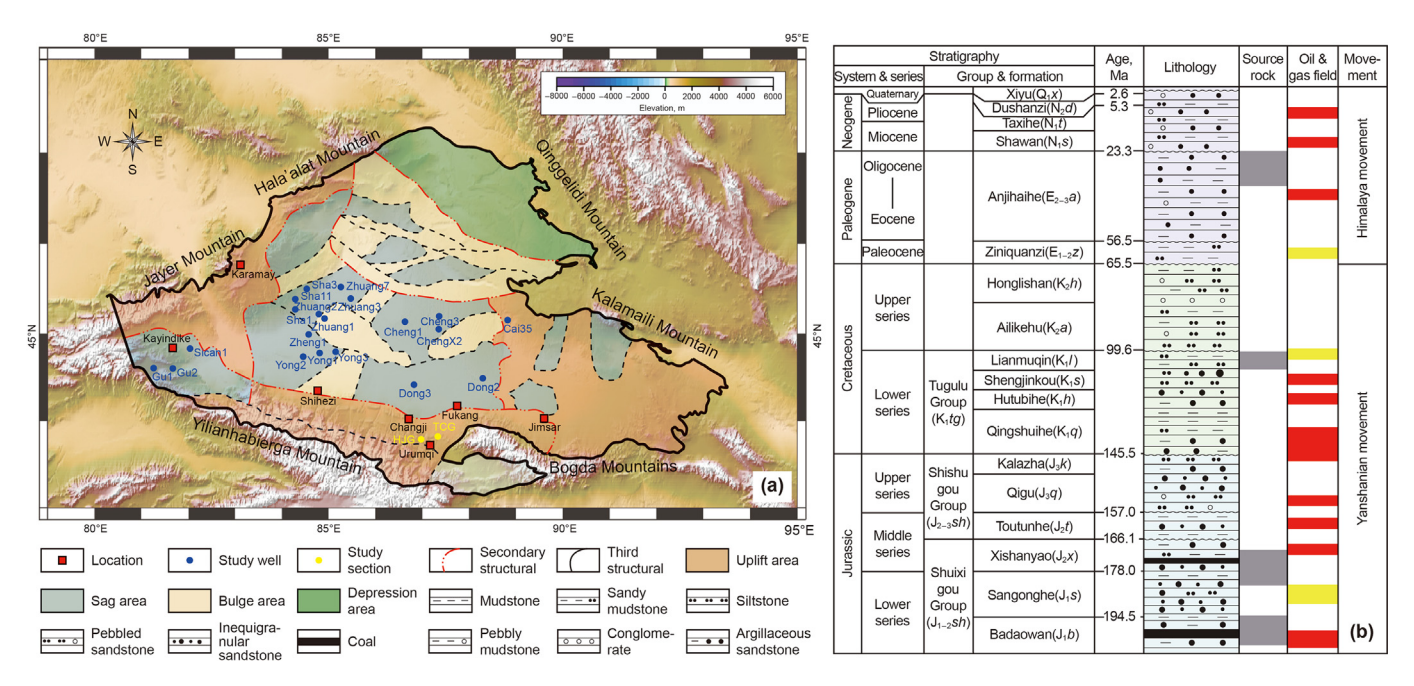


Fig. 1. (a) Structural position and geological section of Junngar Basin and (b) comprehensive stratigraphic column of Junngar Basin.

#### 3.4. Semi-open thermal simulation experiment

The experiments were performed at the Guangzhou Institute of Geochemistry of the Chinese Academy of Sciences. A semi-open pyrolysis experiment allows the control of the pressure inside the reaction system for the continuous expulsion of the products, i.e., oil and gas are generated and discharged simultaneously. Product collection and pyrolysis devices make up the experimental setup, and a stainless-steel oil drain pipe with a 1 mm inner diameter connects the two devices (Fig. 2). Generated gas was collected by the gas cylinder, and the instrument used for the natural gas component test was Agilent 6890 N GC (Hou et al., 2021b; Guo et al., 2022; Huang et al., 2023; Takahashi and Suzuki, 2017; Han et al., 2023). The temperature of the pyrolysis device was increased from an ambient temperature to 200 °C over 2 h and then

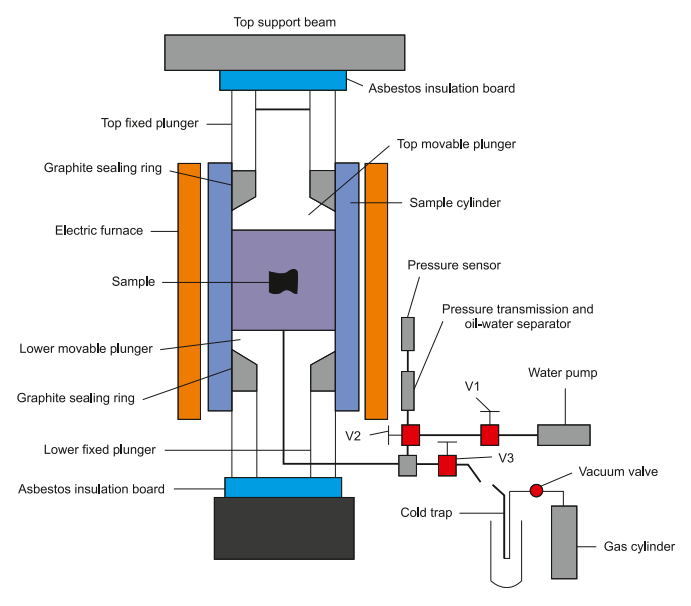


Fig. 2. Schematic diagram of the experimental apparatus.

to pyrolysis temperature at 20 °C/h. The sampling points designed in this study were 300, 320, 340, 360, 380, 400, 420, and 450 °C.

#### 4. Results and discussion

#### 4.1. Pyrolysis characteristics

As listed in Table 1, the TOC values of dark mudstones range from 0.16% to 3.07%, and the  $S_1+S_2$  value ranges from 0.09 to 12.75 mg/g. Moreover, as shown in Fig. 3, N1, N3, N4, and N8 belong to poor source rocks; N7 and N9 to fair source rocks; and N2, N6, N5, and N10 to good source rocks. For the carbonaceous mudstone samples, the TOC values range from 2.29% to 13.79%, and the  $S_1+S_2$ value ranges from 1.62 to 12.61 mg/g, which is higher than that of dark mudstone samples; most of the carbonaceous mudstones are poor to fair source rocks, as shown in Fig. 4. The TOC values of coals span a wide range, and their  $S_1+S_2$  value is less than 120 mg/g, making them poor source rocks, which may be influenced by field washing and weathering. Samples of the same lithology have a wide range of TOC and S<sub>1</sub>+S<sub>2</sub> values, with some having high TOC and low  $S_1+S_2$  or low TOC and high  $S_1+S_2$  values (such as N6 and N10). As shown in Fig. 5, the organic matter types of the different source rocks are mainly II and III, whereas N5 is type I.

Previous studies have demonstrated that when the sample reaches the high-maturity stage, the structural parameter will exhibit opposite trends, which impacts our exploration of the factors influencing hydrocarbon potential (Lis et al., 2005; Bayon et al., 2011; Liu and He, 2017). In this study, the selected samples were in the low-maturity stage, had a maximum pyrolysis temperature ( $T_{\rm max}$ ) of less than 455 °C, and had a  $R_{\rm o}$  value between 0.5% and 1.2%, as shown in Table 1.

# 4.2. Characterization of fourier transform infrared spectroscopy structural parameters

According to the adsorption spectra corresponding to the functional groups, the FTIR absorption spectra can be divided into four regions: aromatic (700–900 cm<sup>-1</sup>), oxygen-containing

**Table 1**Results of Rock-eval/TOC analysis and calculated parameters of samples from three types of source rocks in Junngar Basin.

| Sample ID | Well & location | Depth, m | Formation        | Lithology             | OM type         | TOC, % | S <sub>1</sub> +S <sub>2</sub> , mg/g | HI, mg HC/g TOC | T <sub>max</sub> , °C | R <sub>o,</sub> % |
|-----------|-----------------|----------|------------------|-----------------------|-----------------|--------|---------------------------------------|-----------------|-----------------------|-------------------|
| N1        | Sha11           | 4338.5   | $J_1b$           | Mudstone              | $II_2$          | 1.33   | 1.08                                  | 73.16           | 448                   | 0.82              |
| N2        | Cheng3          | 4484.0   | $J_1b$           | Mudstone              | $II_2$          | 3.07   | 5.02                                  | 136.78          | 447                   | 0.76              |
| N3        | TCG             |          | $J_2x$           | Mudstone              | III             | 0.55   | 0.09                                  | 12.70           | 445                   | 0.86              |
| N4        | Zhuang7         | 4066.0   | $J_1s$           | Mudstone              | $II_2$          | 0.88   | 0.68                                  | 71.60           | 445                   | 0.83              |
| N5        | Sha3            | 3462.0   | $J_1s$           | Mudstone              | I               | 2.52   | 12.75                                 | 500.15          | 444                   |                   |
| N6        | HJG             |          | $J_1b$           | Mudstone              | III             | 3.07   | 0.60                                  | 26.43           | 438                   | 0.52              |
| N7        | Sha1            | 3968.1   | $J_1s$           | Mudstone              | $II_2$          | 1.52   | 2.78                                  | 177.11          | 438                   |                   |
| N8        | HJG             |          | $J_1s$           | Mudstone              | $II_2$          | 1.20   | 0.82                                  | 196.16          | 430                   | 0.53              |
| N9        | HJG             |          | $J_1s$           | Mudstone              | III             | 1.91   | 2.40                                  | 29.79           | 428                   |                   |
| N10       | Dong6           | 5662.5   | $J_1b$           | Mudstone              | III             | 0.16   | 6.46                                  | 99.31           | 419                   |                   |
| TN1       | Cheng1          | 4912.9   | J <sub>1</sub> s | Carbonaceous mudstone | II <sub>1</sub> | 4.10   | 6.69                                  | 156.20          | 451                   | 1.17              |
| TN2       | TCG             |          | $J_1b$           | Carbonaceous mudstone | III             | 13.80  | 5.84                                  | 40.37           | 440                   | 0.62              |
| TN3       | Cheng1          | 4406.8   | $J_2x$           | Carbonaceous mudstone | III             | 3.09   | 2.64                                  | 80.85           | 439                   |                   |
| TN4       | Cheng1          | 4404.5   | $J_2x$           | Carbonaceous mudstone | $II_2$          | 6.92   | 12.61                                 | 178.87          | 439                   | 0.57              |
| TN5       | TCG             |          | $J_2x$           | Carbonaceous mudstone | III             | 13.33  | 5.63                                  | 43.67           | 435                   | 0.53              |
| TN6       | Cheng1          | 4870.1   | $J_1s$           | Carbonaceous mudstone | III             | 2.29   | 1.63                                  | 64.01           | 414                   |                   |
| M1        | HJG             |          | J <sub>1</sub> s | Coal                  | II <sub>2</sub> | 50.90  | 116.75                                | 221.90          | 438                   | 0.52              |
| M2        | HJG             |          | $J_1b$           | Coal                  | III             | 27.80  | 11.72                                 | 41.33           | 424                   | 0.54              |
| M3        | TCG             |          | $J_2x$           | Coal                  | III             | 29.50  | 11.67                                 | 38.38           | 429                   | 0.52              |

**Note:** The spaces mean there is no value here.  $S_1+S_2$ , generation potential, mg HC/g rock;  $T_{max}$ , the temperature of the maximum rate of release of hydrocarbons (corresponding to  $S_2$  peak), °C; TOC, total organic carbon, wt%; HI, hydrogen index ( $S_2 \times 100/\text{TOC}$ ), mg HC/g TOC;  $R_0$ , vitrinite reflectivity, %.

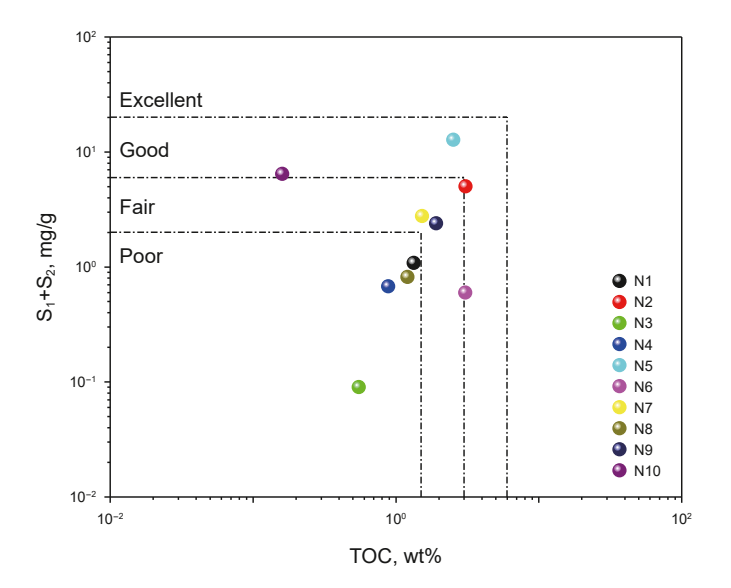
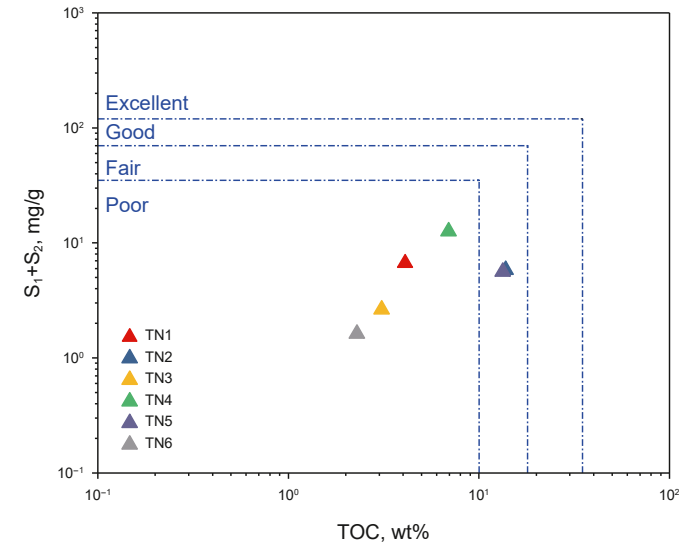


Fig. 3. Plot of  $S_1 + S_2$  values versus TOC contents for mudstones (modified after Chen et al., 1997).



**Fig. 4.** Plot of  $S_1+S_2$  values versus TOC contents for carbonaceous mudstones (modified after Chen et al., 1997).

(1000–1800 cm<sup>-1</sup>), aliphatic (2800–3000 cm<sup>-1</sup>), and hydroxyl (3000–3600 cm<sup>-1</sup>) structure regions (Patterson et al., 1986; Painter et al., 1981; Adams et al., 2005; Cesar and Quintero, 2020). Simultaneous baseline corrections were performed for the aforementioned regions of the selected spectral regions, followed by curve fitting analysis. Based on the shape of the spectral bands, complex spectra are fitted using a combination of Lorentzian and Gaussian functions (as shown in Fig. 6; take sample N1 as an example). The curve-fitted spectra can then be used to determine the FTIR parameters.

The FTIR curves of the three different types of source rocks obtained after baseline correction are shown in Figs. 7–9, and the results indicate that the adsorption peaks of each type share a similar morphology, suggesting that they have a similar functional group structure. It can be seen that the spectra are characterized by strong aliphatic C–H stretching bands from 2800 to 3000 cm<sup>-1</sup>, strong intensities of aromatic (C=C) stretching vibration near

1600 cm<sup>-1</sup>, and the strongest intensities of C–O stretching from 1000 to 1300 cm<sup>-1</sup>. However, the peak heights and areas of the adsorption peaks are quite different. As shown in Fig. 10, the relative value of the area for the absorption peak of the aromatic structure gradually increases from dark mudstone to coal, and there is not much change in the relative value of the area for the absorption peak of the aliphatic structure.

Previous studies showed that the predominantly aromatic and aliphatic structures associated with the composition of organic matter in hydrocarbon source rocks (Patterson et al., 1986; Ibarra et al., 1996; Marshall et al., 2001; Wang et al., 2011, 2016; Pan et al., 2023) proved that the characteristics of the aliphatic functional group areas of kerogen are consistent with those of the source rocks. Thus, we mainly analyzed the aliphatic and aromatic structures, and selected the aromatic structure parameters, apparent aromaticity  $f_a$ , aromatic abundance parameters I, and degree of condensation DOC (Chen et al., 2014; Zhou et al., 2015; Liu

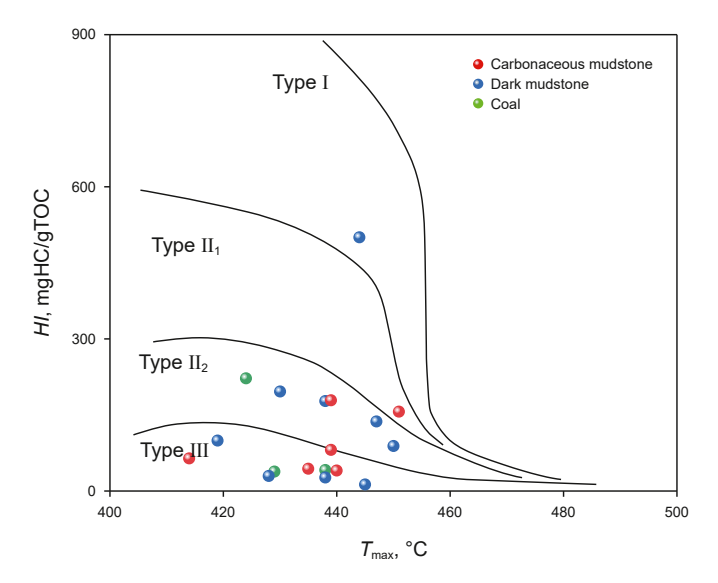


**Fig. 5.** Plots of HI versus  $T_{\text{max}}$  values for coal-measure source rocks (modified after Cornford et al., 1998).

et al., 2016; He et al., 2017), and aliphatic structure parameters, intensity ratio of  $-CH_2/-CH_3$  (A ( $CH_2$ )/A ( $CH_3$ )), and aliphatic hydrogen enrichment parameters H, and aliphatic relative

abundance factor A (Gu et al., 2014; Liu et al., 2016) as research focus.

 $f_{\rm a}$  is an aromatic structure parameter, representing the fraction of carbon atoms in the aromatic structure (Wang et al., 2011; Zhang et al., 2021). This parameter is mainly calculated as follows:

$$f_{\rm a} = 1 - \left( \frac{A_{2800-3000}}{A_{2800-3000} + A_{700-900}} \times \frac{H}{C} \right) / 1.8 \tag{1}$$

where  $A_{2800-3000}$  and  $A_{700-900}$  correspond to the integrated peak area of 2800–3000 and 700–900 cm<sup>-1</sup>, respectively. H/C is the concentration ratio of hydrogen atoms to carbon atoms.

*I* characterizes the coal grade and aromaticity and can be used to compare the relative abundance of aromatic and aliphatic functional groups (Zhou et al., 2015; He et al., 2017). This parameter is calculated as follows:

$$I = \frac{A_{700-900}}{A_{2800-3000}} \tag{2}$$

DOC denotes the level of condensation of the aromatic ring in the macromolecular system and is related to the area of the corresponding integral peak at 1600 cm<sup>-1</sup> in the spectrum (Liu et al., 2016; He et al., 2017), which represents the intensity of the aromatic ring; it is calculated as follows:

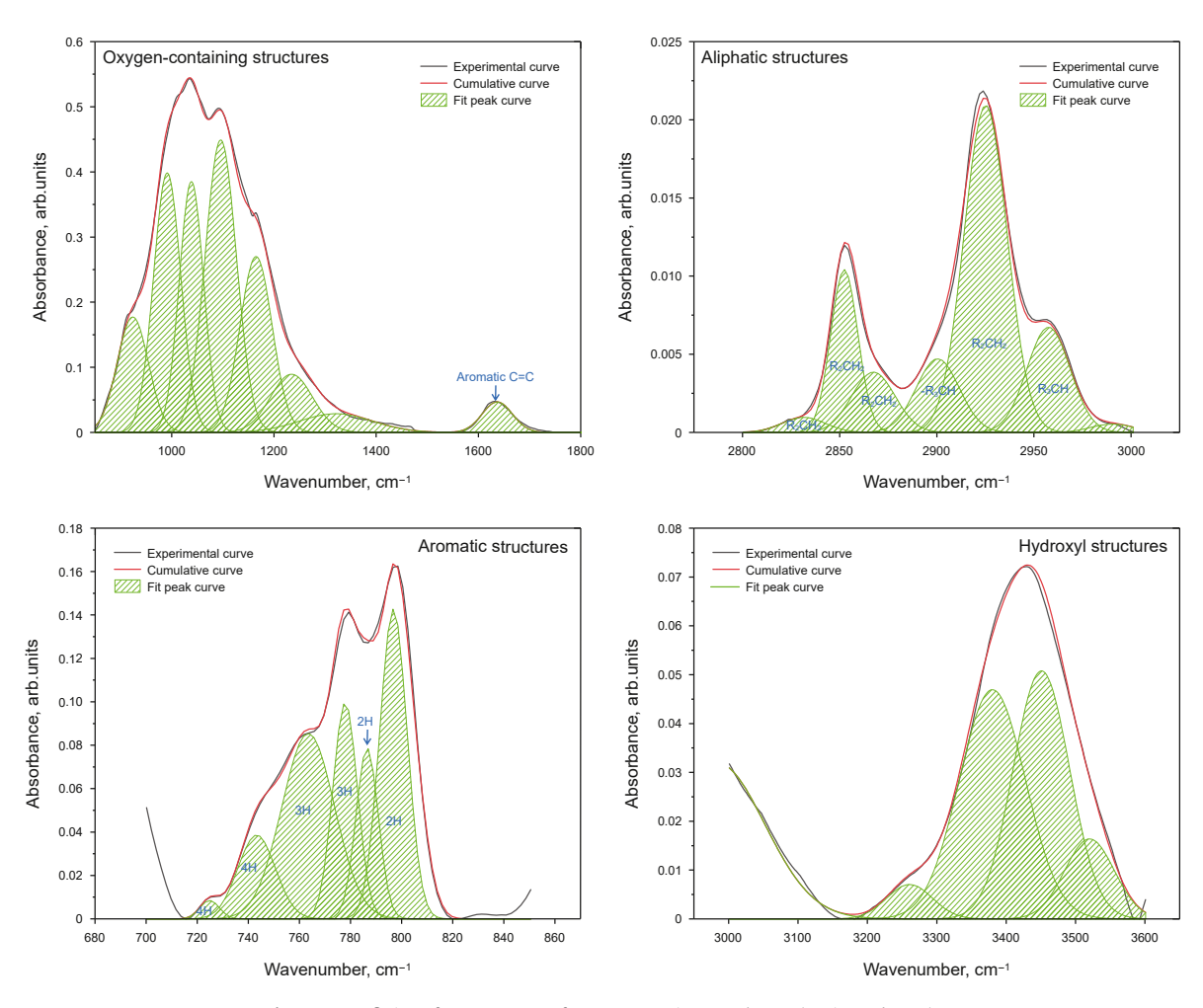


Fig. 6. Curve fitting of FTIR spectrum for representative samples N1 (N1 is mudstone).

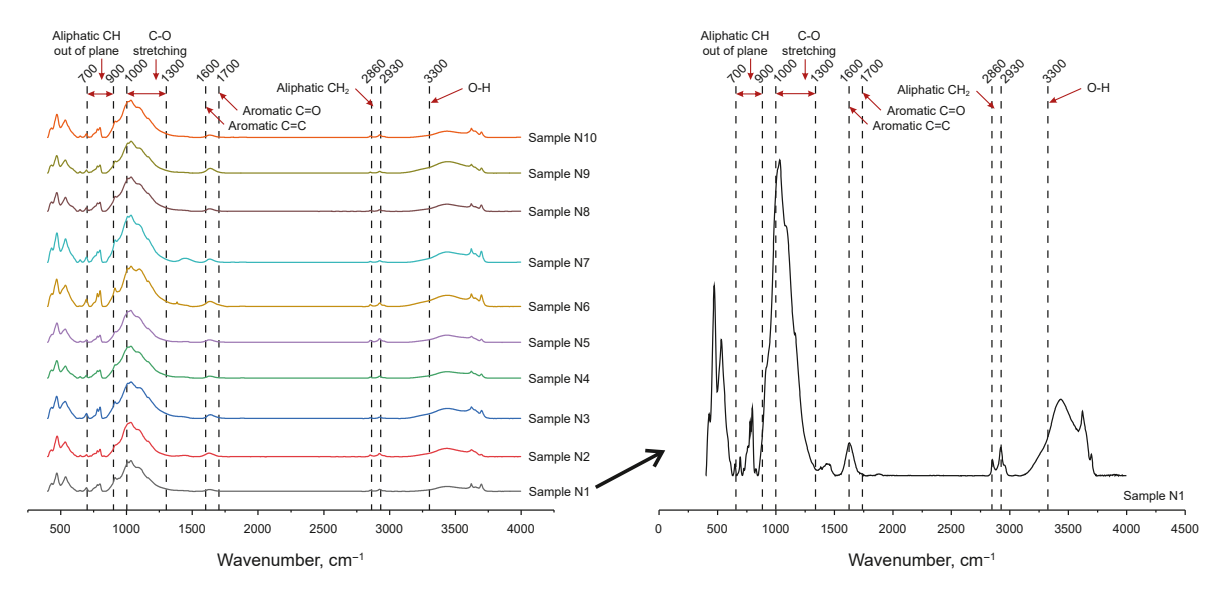


Fig. 7. FTIR curves of mudstone samples (including samples N1-N10).

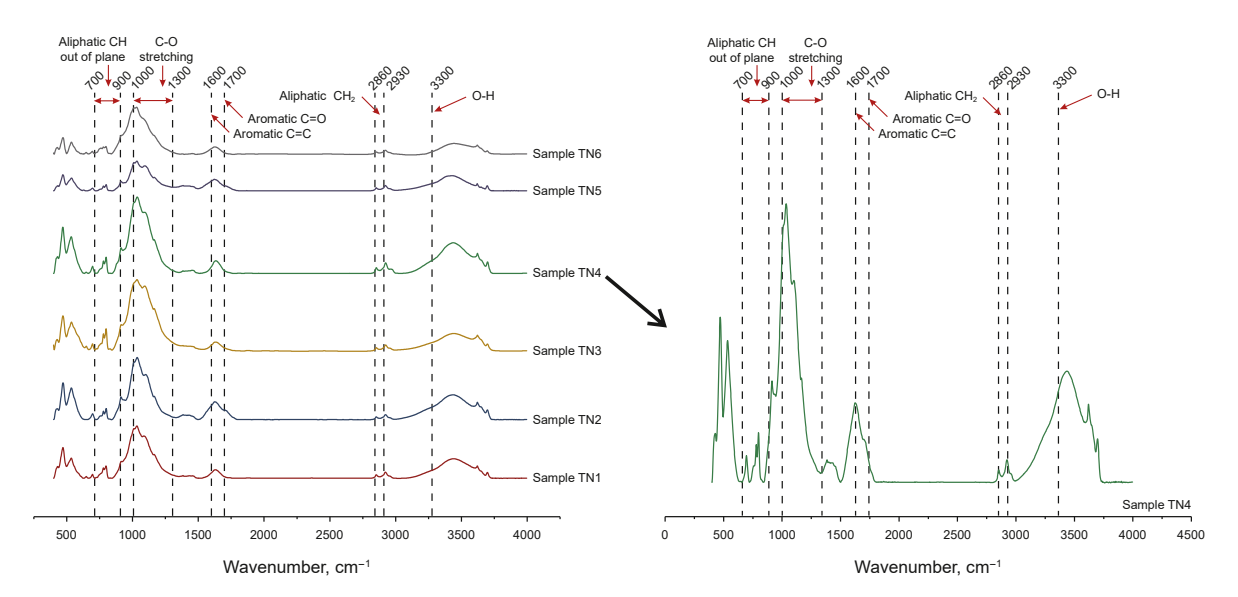


Fig. 8. FTIR curves of carbonaceous mudstone samples (including samples TN1-TN6).

$$DOC = \frac{A_{700-900}}{A_{1600}} \tag{3}$$

where  $A_{700-900}$  and  $A_{1600}$  correspond to the integrated peak area of 2800-3000 and  $1600~\rm{cm}^{-1}$ , respectively.

A (CH<sub>2</sub>)/A (CH<sub>3</sub>) characterizes the fat chain length and degree of branched chaining; the greater is the value of this parameter, the longer and less branched are the fat chains of the samples (Zhou et al., 2015; Liu et al., 2016). The  $-CH_2$  to  $-CH_3$  intensity ratio can be obtained using the following equation:

$$\frac{A(\text{CH}_2)}{A(\text{CH}_3)} = \frac{A_{2915-2940}}{A_{2950-3000}} \tag{4}$$

*H* is merged with hydrogen-rich parameters from earlier studies (Guo et al., 2014) and is mainly utilized to respond to the relative abundance of C–H bonds in aliphatic groups; it is calculated as follows:

$$H = \frac{A_{2900-3000}}{A_{2900-3000} + A_{700-900}} \tag{5}$$

*A* represents the enrichment of the aliphatic group and is calculated as follows:

$$A = \frac{A_{2800-3000}}{A_{2800-3000} + A_{1600}} \tag{6}$$

The FTIR spectra were peaked and fitted using the Origin8.5 software, and the fitted peaks were calculated for each spectral range; the fitting results indicated that the fit of each sample's FTIR spectra was more than 0.98 (Fig. 6). On this basis, the value of related parameters was calculated using Eqs. (1)—(6).

The results are presented in Figs. 11 and 12, and Table 2. For the aromatic structure parameters, the results indicate that the dark mudstone has the highest  $f_a$  value (between 0.77 and 0.92, with an average of 0.87), followed by carbonaceous mudstone (between

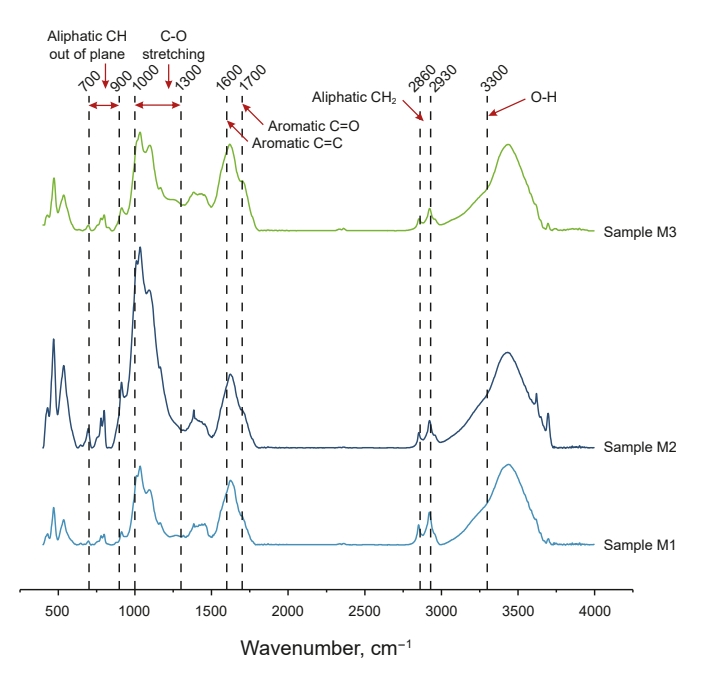
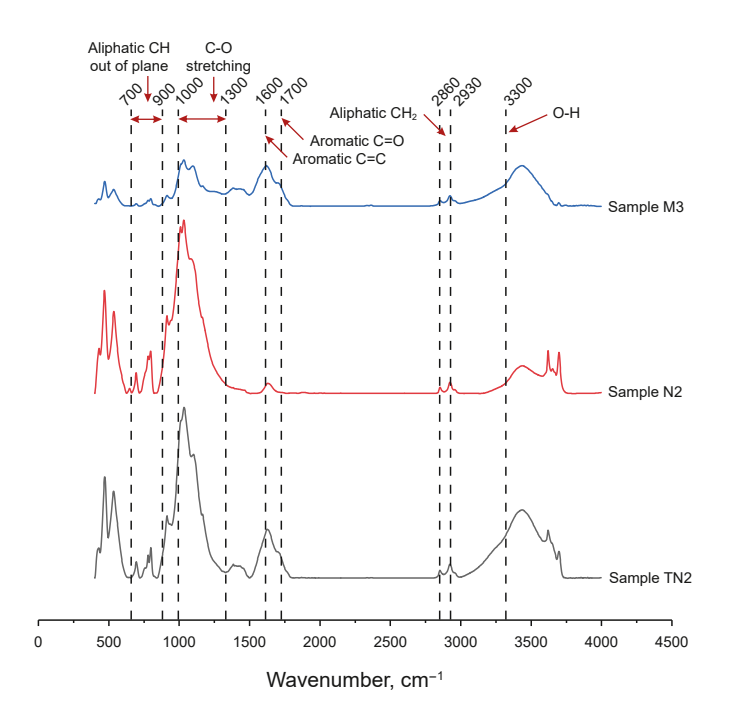
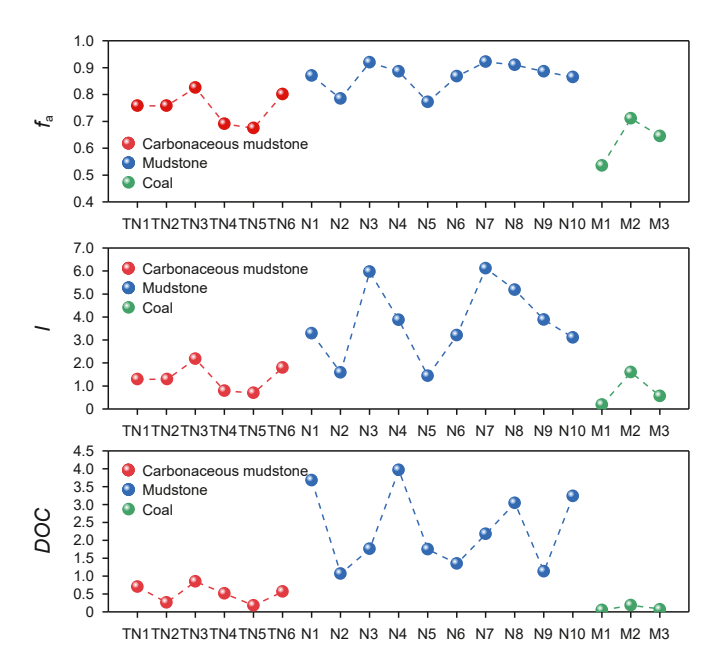


Fig. 9. FTIR curves of coal samples (including samples M1-M3).

0.67 and 0.83, with an average of 0.75) and then coal. This shows that the fraction of carbon atoms in the aromatic structure of coal is lower, whereas that of the dark mudstone is higher. The distribution of the I value is similar to that of the  $f_a$  value, which also shows that dark mudstone > carbonaceous mudstone > coal, indicating that the proportion of aromatic functional groups in coal and carbonaceous mudstone is lower than that in dark mudstone. The DOC value shows that the aromatic structure of dark mudstone has a higher DOC than that of the other two types, suggesting that it is more antioxidant and more stable.



**Fig. 10.** Comparison of FTIR curve characteristics of three different types (mudstone: N2; carbonaceous mudstones: TN2; coal: M3) of source rocks.



**Fig. 11.** Distribution characteristics of aromatic structural parameters for three types of source rocks.

For the aliphatic structure parameters, coal has relatively low A values, ranging from 0.11 to 0.22, indicating a relatively high aliphatic abundance of coal. However, the H value of coal is considerably higher than that of the other two types, with values ranging from 0.56 to 0.83 (average 0.67), indicating that the aliphatic structure of coal contains a comparatively high proportion of C—H bonding structures, suggesting that coal is comparatively rich in hydrogen. The A (CH<sub>2</sub>)/A (CH<sub>3</sub>) values indicate that coal is the most branched, followed by dark mudstone, showing that coal is richer in aliphatic structures with methyl compounds.

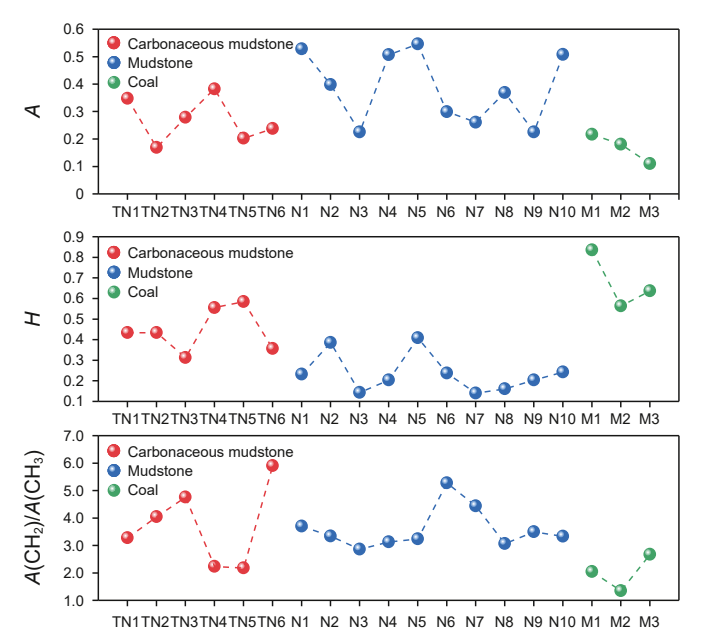


**Fig. 12.** Distribution characteristics of aliphatic structural parameters for three types of source rocks.

**Table 2**Calculation of molecular structure parameters of samples from three types of source rocks in Junngar Basin.

| Sample ID | Well & location | Depth, m | Formation        | Lithology             | DOC  | I    | $f_{a}$ | A (CH <sub>2</sub> )/A (CH <sub>3</sub> ) | Н    | A    |
|-----------|-----------------|----------|------------------|-----------------------|------|------|---------|---|------|------|
| N1        | Sha11           | 4338.5   | $J_1b$           | Mudstone              | 3.68 | 3.29 | 0.87    | 3.71                                      | 0.23 | 0.53 |
| N2        | Cheng3          | 4484.0   | $J_1b$           | Mudstone              | 1.07 | 1.61 | 0.79    | 3.35                                      | 0.39 | 0.40 |
| N3        | ZZS             |          | $J_2x$           | Mudstone              | 1.76 | 6.05 | 0.92    | 2.87                                      | 0.14 | 0.23 |
| N4        | Zhuang7         | 4066.0   | $J_1s$           | Mudstone              | 3.97 | 3.86 | 0.89    | 3.13                                      | 0.20 | 0.51 |
| N5        | Sha3            | 3462.0   | $J_1s$           | Mudstone              | 1.75 | 1.45 | 0.77    | 3.25                                      | 0.41 | 0.55 |
| N6        | HJG             |          | $J_1b$           | Mudstone              | 1.36 | 3.17 | 0.87    | 5.28                                      | 0.24 | 0.19 |
| N7        | Sha1            | 3968.1   | $J_1s$           | Mudstone              | 2.18 | 6.17 | 0.92    | 4.45                                      | 0.14 | 0.26 |
| N8        | HJG             |          | $J_1s$           | Mudstone              | 3.05 | 5.20 | 0.91    | 3.07                                      | 0.16 | 0.37 |
| N9        | HJG             |          | $J_1s$           | Mudstone              | 1.13 | 3.88 | 0.89    | 3.51                                      | 0.20 | 0.23 |
| N10       | Dong6           | 5662.5   | $J_1b$           | Mudstone              | 3.24 | 3.13 | 0.86    | 3.33                                      | 0.24 | 0.51 |
| TN1       | Cheng1          | 4912.9   | J <sub>1</sub> s | Carbonaceous mudstone | 0.71 | 1.32 | 0.76    | 3.29                                      | 0.43 | 0.35 |
| TN2       | TCG             |          | $J_1b$           | Carbonaceous mudstone | 0.27 | 1.30 | 0.76    | 4.05                                      | 0.43 | 0.19 |
| TN3       | Cheng1          | 4406.8   | $J_2x$           | Carbonaceous mudstone | 0.85 | 2.21 | 0.83    | 4.77                                      | 0.31 | 0.28 |
| TN4       | Cheng1          | 4404.5   | $J_2x$           | Carbonaceous mudstone | 0.52 | 0.84 | 0.69    | 2.24                                      | 0.56 | 0.38 |
| TN5       | TCG             |          | $J_2x$           | Carbonaceous mudstone | 0.18 | 0.71 | 0.67    | 2.18                                      | 0.59 | 0.20 |
| TN6       | Cheng1          | 4870.1   | $J_1s$           | Carbonaceous mudstone | 0.57 | 1.83 | 0.80    | 5.91                                      | 0.36 | 0.24 |
| M1        | HJG             |          | J <sub>1</sub> s | Coal                  | 0.05 | 0.20 | 0.71    | 2.05                                      | 0.84 | 0.22 |
| M2        | HJG             |          | $J_1b$           | Coal                  | 0.30 | 1.35 | 0.54    | 2.50                                      | 0.47 | 0.17 |
| M3        | TCG             |          | $J_2x$           | Coal                  | 0.07 | 0.57 | 0.65    | 2.68                                      | 0.64 | 0.11 |

**Note:** The spaces mean there is no value here.

# 4.3. Influence of molecular structure characteristics on hydrocarbon potential

Because of the differences in the molecular structure of coalmeasure source rocks, we investigated the relationship between the characteristics associated with the hydrocarbon potential of source rocks and their molecular structure parameters by lithology; and the correlation results are presented in Figs. 13–16.

Fig. 13 shows that most of the aromatic structural parameters are negatively correlated with the organic matter abundance parameters. Among the three lithologies, when the *I* value is higher, the  $S_1+S_2$  and TOC values of the samples are lower, indicating that the organic matter abundance and pyrolytic hydrocarbons of the hydrocarbon source rock are higher when the percentage of the aliphatic structure content is higher and the percentage of the aromatic structure content is lower. Regarding  $f_a$ , overall, as the  $S_1+S_2$ and TOC values of the samples increase, the  $f_a$  value decreases, clearly showing the correlation between  $f_a$  and TOC, which indicates that the level of carbon atom fraction in the aromatic structure is mainly related to the TOC value of coal-measure source rocks. The DOC values have no significant linear correlation with the  $S_1+S_2$  and TOC values, but in general, samples with high  $S_1+S_2$ and TOC values have lower DOC values, proving that the lower is the DOC of the aromatic structure, the higher is the abundance of organic matter in source rocks and the better is its quality. In summary, when the coal-measure source rock has a high abundance of organic matter, its aromatic structure should have a lower DOC, carbon fraction, and proportion of its aromatic structure.

Fig. 14 shows that, except for the H value, the aliphatic characteristics have a weak association with the hydrocarbon potential parameters. Fig. 14(c) and (d) demonstrate that the A (CH<sub>2</sub>)/A (CH<sub>3</sub>) value in carbonaceous mudstone samples has a significant negative correlation with the pyrolysis parameters, indicating that as the aliphatic methyl group increases and the methylene group decreases, the hydrocarbon production of carbonaceous mudstone increases. In all three types of source rocks, the H values exhibit a substantial positive correlation with  $S_1+S_2$  and TOC. This implies that the hydrocarbon potential of source rocks increases as the percentage of aliphatic hydrocarbon structure increases. That is, the influence of aliphatic structure on the hydrocarbon potential of source rocks is reflected in the fraction of total aliphatic C-H bonds, whereas the remainder of the influence on the hydrocarbon

potential is rather negligible. Furthermore, as presented in Figs. 13 and 14, the aromatic structural parameters are more correlated with the TOC values whereas the aliphatic structural parameters are more correlated with the  $S_1+S_2$  values.

Figs. 15 and 16 show that when the organic matter type is better, the value of aliphatic abundance factor *A* is higher. The *A* value of mudstone is higher than those of carbonaceous mudstone and coal for the same organic matter type. The organic matter type and the rest of the parameters do not appear to be related. This implies that the organic matter type of coal–measure source rocks is correlated with aliphatic abundance factor *A*, indicating that the higher is the organic matter type, the higher is the *A* value.

Fig. 17 presents the relationship between molecular structure parameters and the value of  $T_{\rm max}$ . Overall, there is no substantial correlation between the molecular structure parameters and  $T_{\rm max}$  for carbonaceous mudstones and mudstones. For coals, the *DOC* and *I* values exhibit a weak positive correlation with  $T_{\rm max}$ , whereas the *H* values show a substantial negative correlation with  $T_{\rm max}$ , indicating that as the maturity of coal increases, the condensation of its aromatic structure increases and the relative abundance of the fatty structure considerably decreases.

In summary, the organic macromolecular structure is closely related to various hydrocarbon potential parameters. The quality of coal–measure source rocks will be the highest when the *DOC*, fraction of carbon atoms, and overall percentage of aromatic structure are low and the percentages of aliphatic structure and C–H bonding are high.

# 4.4. Discussion of the semi-open pyrolysis results from the molecular structure

We selected different types of coal–measure source rocks (N6, TN2, M2) from the same area (southern edge of Junggar Basin) and formation  $(J_1b)$  to conduct thermal simulation experiments in a semi-open system. Table 3 presents the basic information and characteristics of the structure parameters of the samples.

The semi-open pyrolysis experiments revealed that while the yield trends of the different products from each of the three types of source rocks were comparable, the yield among the different products varied. Fig. 18(a)–(c) show the variations in the yield of gaseous  $(C_1$ – $C_5)$ , light  $(C_6$ – $C_{14})$ , and heavy  $(C_{14+})$  hydrocarbons. Fig. 18(a) illustrates how the gaseous hydrocarbon yield of the

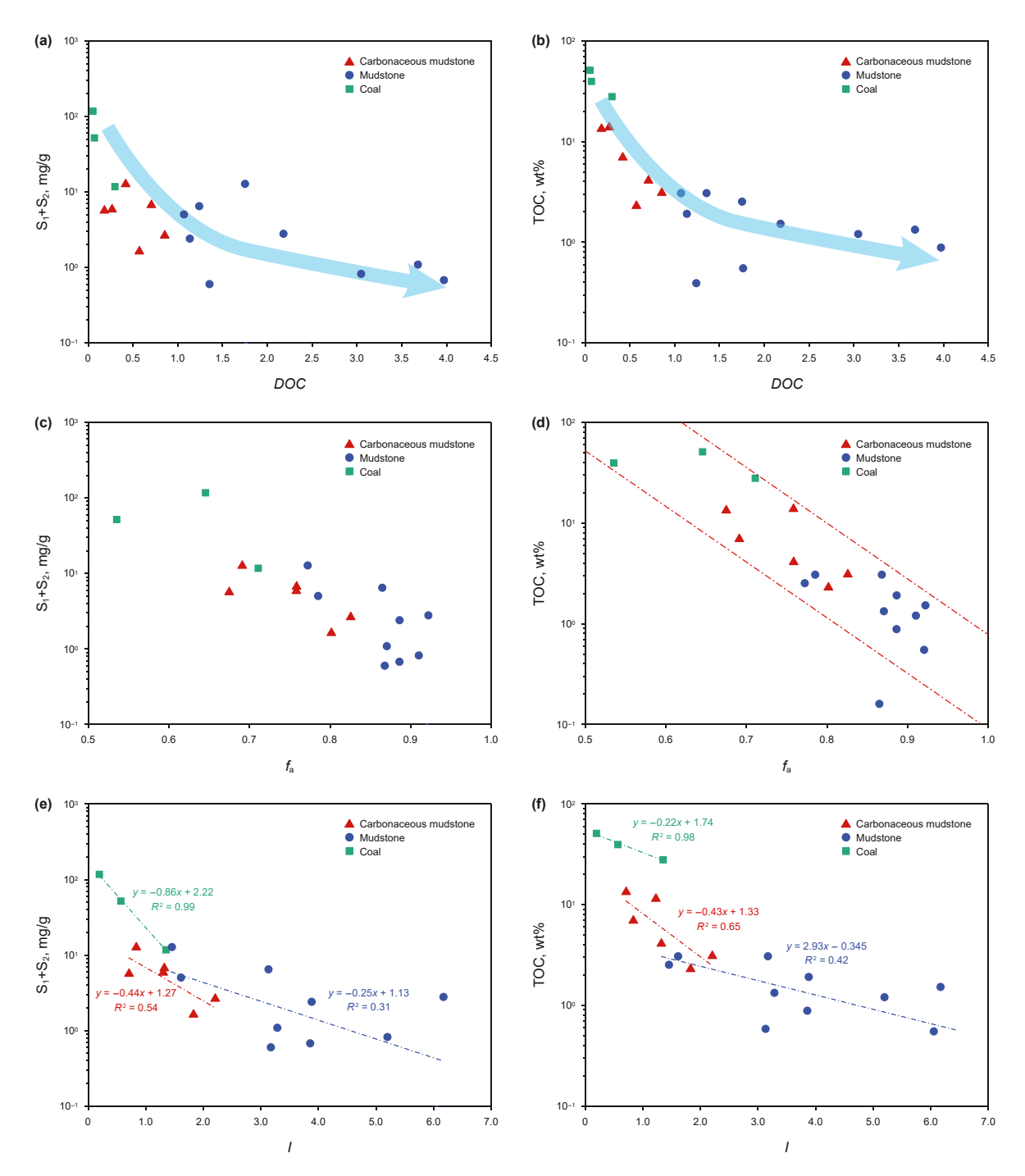
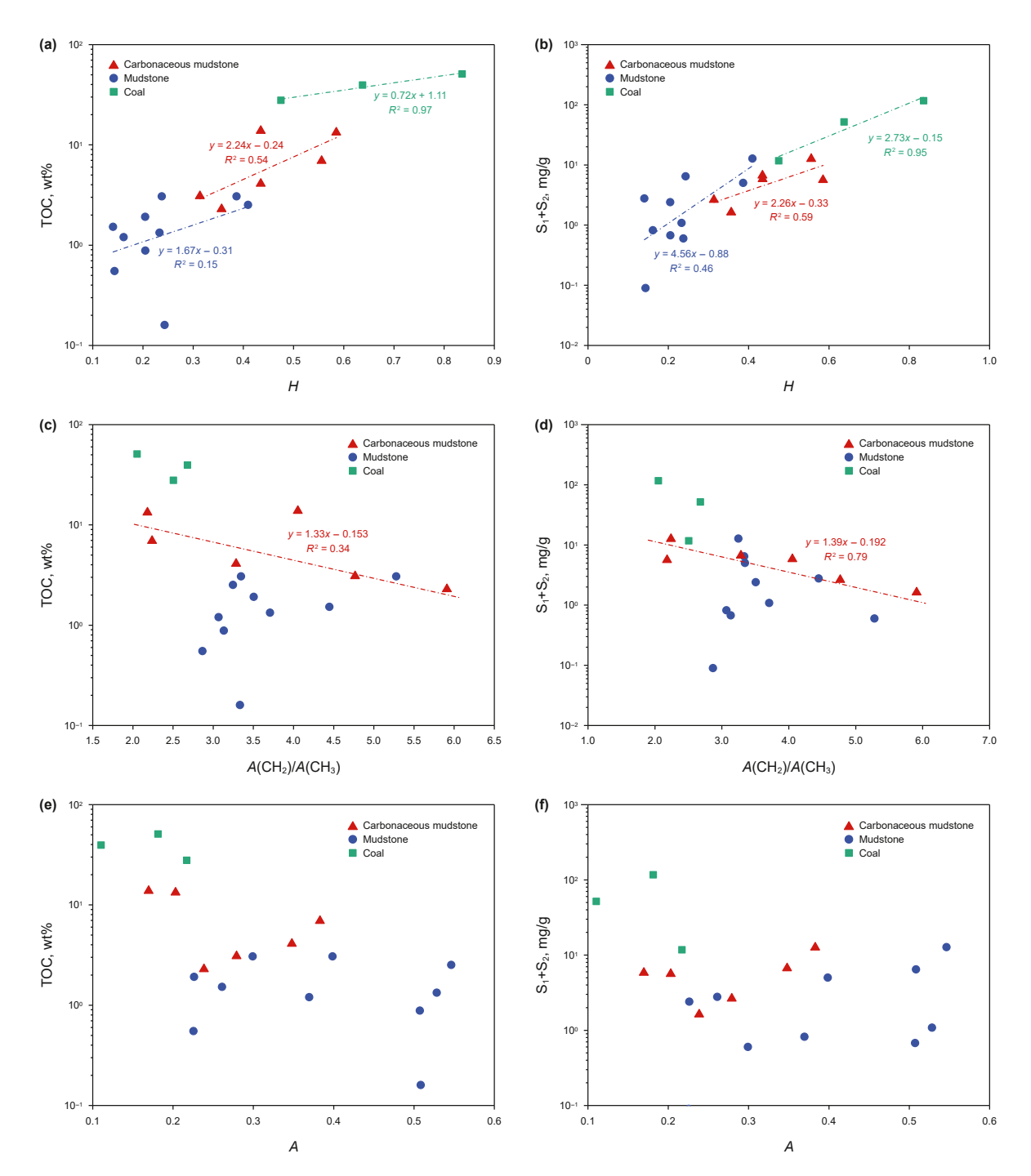
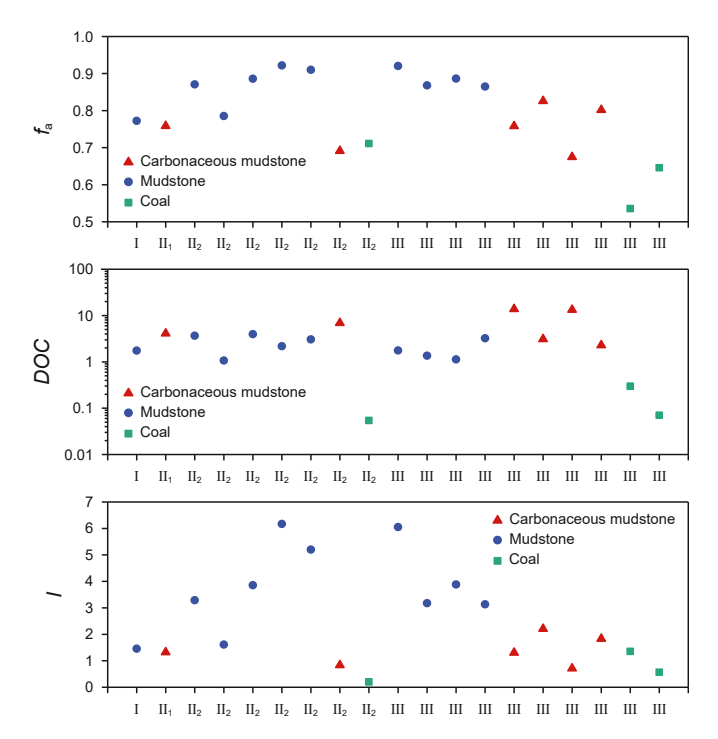


Fig. 13. Cross—plots of (a) DOC versus S<sub>1+</sub>S<sub>2</sub>, (b) DOC versus TOC, (c) f<sub>a</sub> versus S<sub>1+</sub>S<sub>2</sub>, (d) f<sub>a</sub> versus TOC, (e) I versus S<sub>1+</sub>S<sub>2</sub>, (f) I versus TOC for coal—measure source rocks.



**Fig. 14.** Cross—plots of **(a)** *H* versus TOC, **(b)** *H* versus S<sub>1</sub>+S<sub>2</sub>, **(c)** *A* (CH<sub>2</sub>)/*A* (CH<sub>3</sub>) versus TOC, **(d)** *A* (CH<sub>3</sub>) versus S<sub>1</sub>+S<sub>2</sub>, **(e)** *A* versus TOC, **(f)** *A* versus S<sub>1</sub>+S<sub>2</sub> for coal—measure source rocks.



**Fig. 15.** Distribution of aromatic parameters according to the type of organic matter in the three types of source rocks.

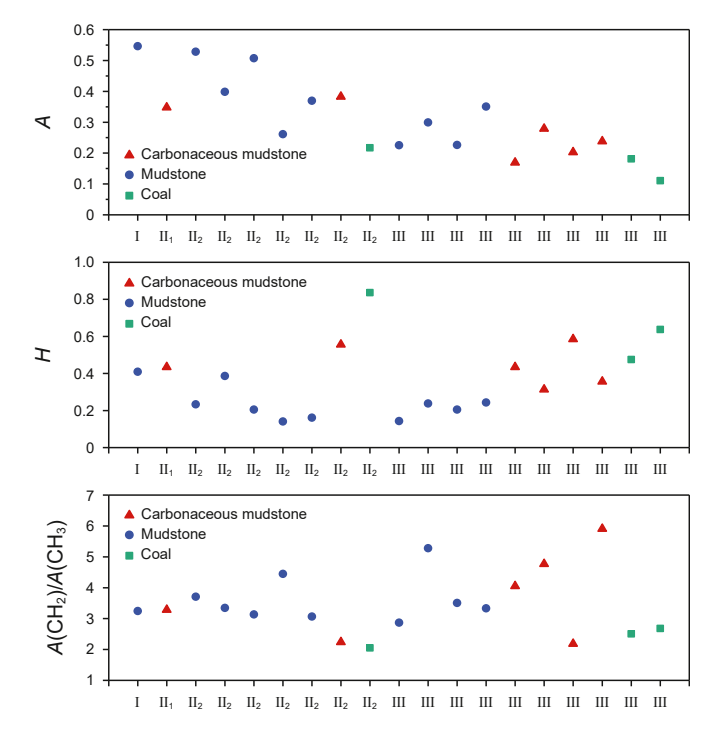


**Fig. 16.** Distribution of aliphatic parameters according to the type of organic matter in the three types of source rocks.

samples increased as the temperature increased, and they are roughly characterized as coal > carbonaceous mudstone > dark mudstone. Before 380 °C (corresponding to 0.93%  $R_0$ ), the gaseous

hydrocarbon production rate slowly increases and reaches the first inflection point at 380 °C, after which the gaseous hydrocarbon production rate increases faster. For carbonaceous mudstone, its gaseous hydrocarbon production rate reaches the second inflection point at 420 °C (corresponding to 1.34%  $R_0$ ). This indicates that the first important stage of the rapid production of gaseous hydrocarbons in carbonaceous mudstone occurs between 380 °C and 420 °C. which is the hydrocarbon gas stage of the tyrosine degradation. The stage of the cracked gas has not yet been reached, and the hydrocarbon gas stage of the tyrosine degradation of the mudstone and coal begins at 380 °C. Fig. 18(c) demonstrates that coal has the highest heavy hydrocarbon yield, with an inflection point at 420 °C, indicating that heavy hydrocarbons crack when the temperature is increased further. Fig. 18(b) shows that carbonaceous mudstone has the highest light hydrocarbon yield. The light hydrocarbon yield is substantially higher than the yields of gaseous and heavy hydrocarbons for all lithologies, and dominated the trends in total production

The findings of earlier studies on coal-measure source rock differ from the findings of the present study (Yang et al., 2021; Yu et al., 2022). According to the pyrolysis parameters of coal and carbonaceous mudstone, coal should have the highest hydrocarbon production capacity, but if it is based on the quality evaluated according to the evaluation criteria the mudstone should have the highest hydrocarbon production capacity. Therefore, it is possible that another factor is influencing the hydrocarbon potential of the coal-measure source rocks.

From organic molecular structure perspective, the above phenomenon can be well explained as follows (Table 3): (1) According to the A (CH<sub>2</sub>)/A (CH<sub>3</sub>) values, mudstone has the highest A (CH<sub>2</sub>)/A (CH<sub>3</sub>) value, followed by carbonaceous mudstone and coal, indicating that the carbon chain in coal is the shortest; moreover, the proportion of methyl content is extremely high. Therefore, when the pyrolysis process occurs, the coal will have more -CH<sub>3</sub> to fracture to form methane compared to carbonaceous mudstone and mudstone, coal should show a high value of the gaseous hydrocarbon yield, and the process of gaseous hydrocarbon production is the longest. (2) The H value of coal is slightly higher than that of carbonaceous mudstone, but the DOC, I, and A values show that the aromatic system of carbonaceous mudstone has a lower DOC and a higher proportion of aliphatic structure; this implies that carbonaceous mudstones have a slightly higher potential to produce hydrocarbons than coal. (3) For the phenomenon of higher heavy hydrocarbon yield in coal rock, the proportion of the "-CH-" structure can be used to explain, it can be calculated by the following formula: percentage of "-CH-" =  $A_{2900}/A_{2800-3000}$ , where  $A_{2800-3000}$  and  $A_{2900}$  correspond to the integrated peak area of 2800–3000 and 2900 cm<sup>-1</sup> respectively. Using this formula, the percentage of "-CH-" in coal was calculated to be 19.5% vs. 14.4% in carbonaceous mudstone, indicating that the structure of the aliphatic C-chain has more branches and is more complex in coal. Combined with the high DOC of the aromatic system of coal, the structure of the aromatic group in coal is also more complex. The number of carbon atoms in the product after the long-chain breakage is still higher; hence, its heavy hydrocarbon yield is higher than mudstone and carbonaceous mudstone.

In summary, the molecular structure efficiently explains the simulation results of the semi-open pyrolysis experiments, demonstrating the close relationship between the molecular structure and the hydrocarbon potential of coal-measure source rocks. The molecular structure can be combined when evaluating the good or bad quality of coal-measure source rocks.

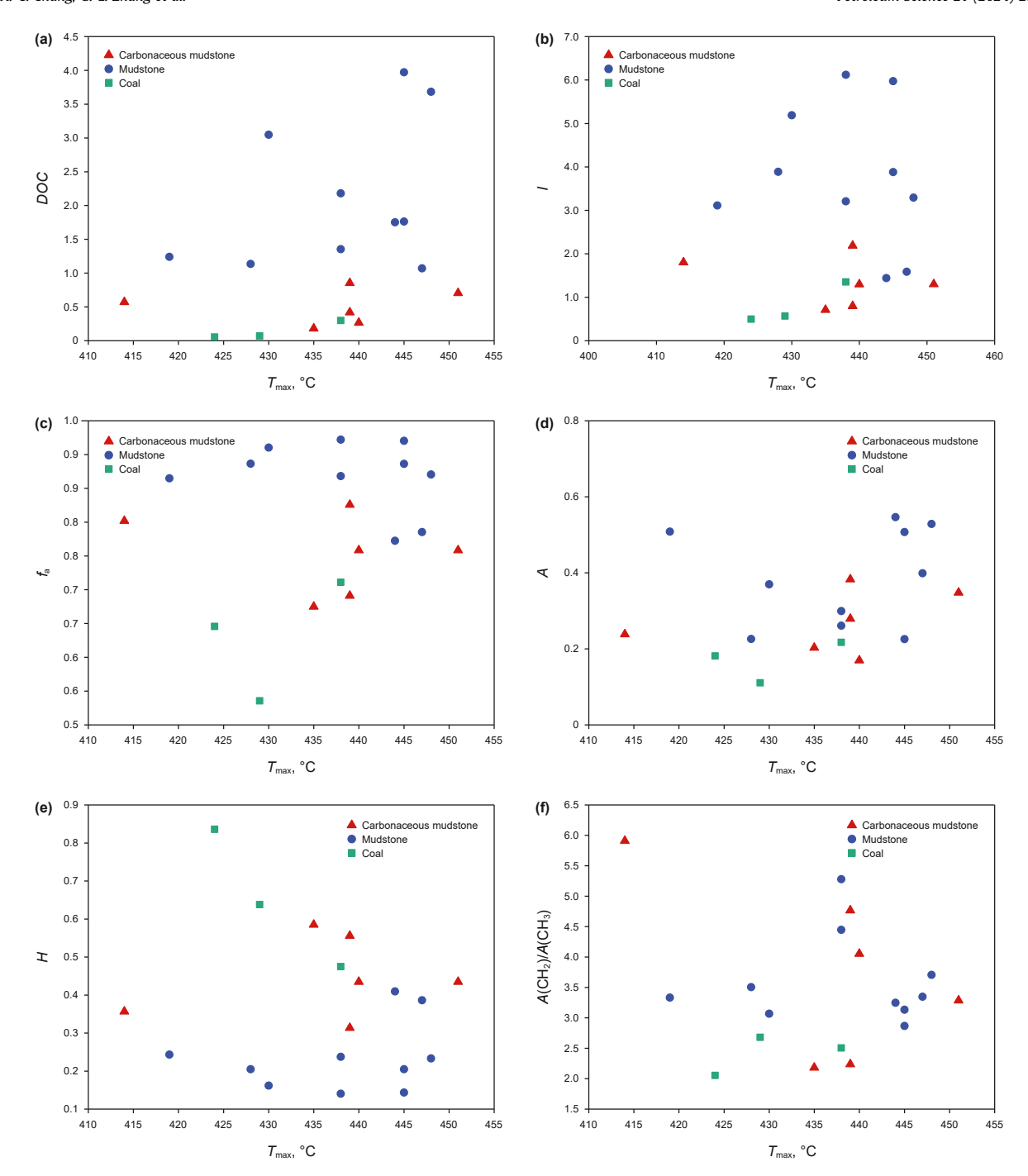


Fig. 17. Cross—plots of (a) DOC versus  $T_{\max}$ . (b) I versus  $T_{\max}$ . (c)  $f_a$  versus  $T_{\max}$ . (d) A versus  $T_{\max}$ . (e) H versus  $T_{\max}$ . (f) A (CH<sub>2</sub>)/A (CH<sub>3</sub>) versus  $T_{\max}$  for coal—measure source rocks.

**Table 3**Characterization of basic parameters of experimental samples for semi-open thermal simulation.

| Sample ID | Well & location | Formation | Lithology             | Pyrolysis parameter |        |                    | Molecular structure parameter |      |      |             |   |      |      |
|-----------|-----------------|-----------|-----------------------|---------------------|--------|--------------------|-------------------------------|------|------|-------------|---|------|------|
|           |                 |           |                       | OM type             | TOC, % | $S_1+S_2$ , $mg/g$ | T <sub>max</sub> , °C         | DOC  | I    | $f_{\rm a}$ | A (CH <sub>2</sub> )/A (CH <sub>3</sub> ) | Н    | Α    |
| N6        | HJG             | $J_1b$    | Mudstone              | III                 | 3.07   | 0.60               | 438                           | 1.36 | 3.17 | 0.87        | 5.28                                      | 0.24 | 0.19 |
| TN2       | TCG             | $J_1b$    | Carbonaceous mudstone | III                 | 13.80  | 5.84               | 440                           | 0.27 | 1.30 | 0.76        | 4.05                                      | 0.43 | 0.19 |
| M2        | HJG             | $J_1b$    | Coal                  | III                 | 27.80  | 11.72              | 424                           | 0.30 | 1.35 | 0.54        | 2.50                                      | 0.47 | 0.17 |

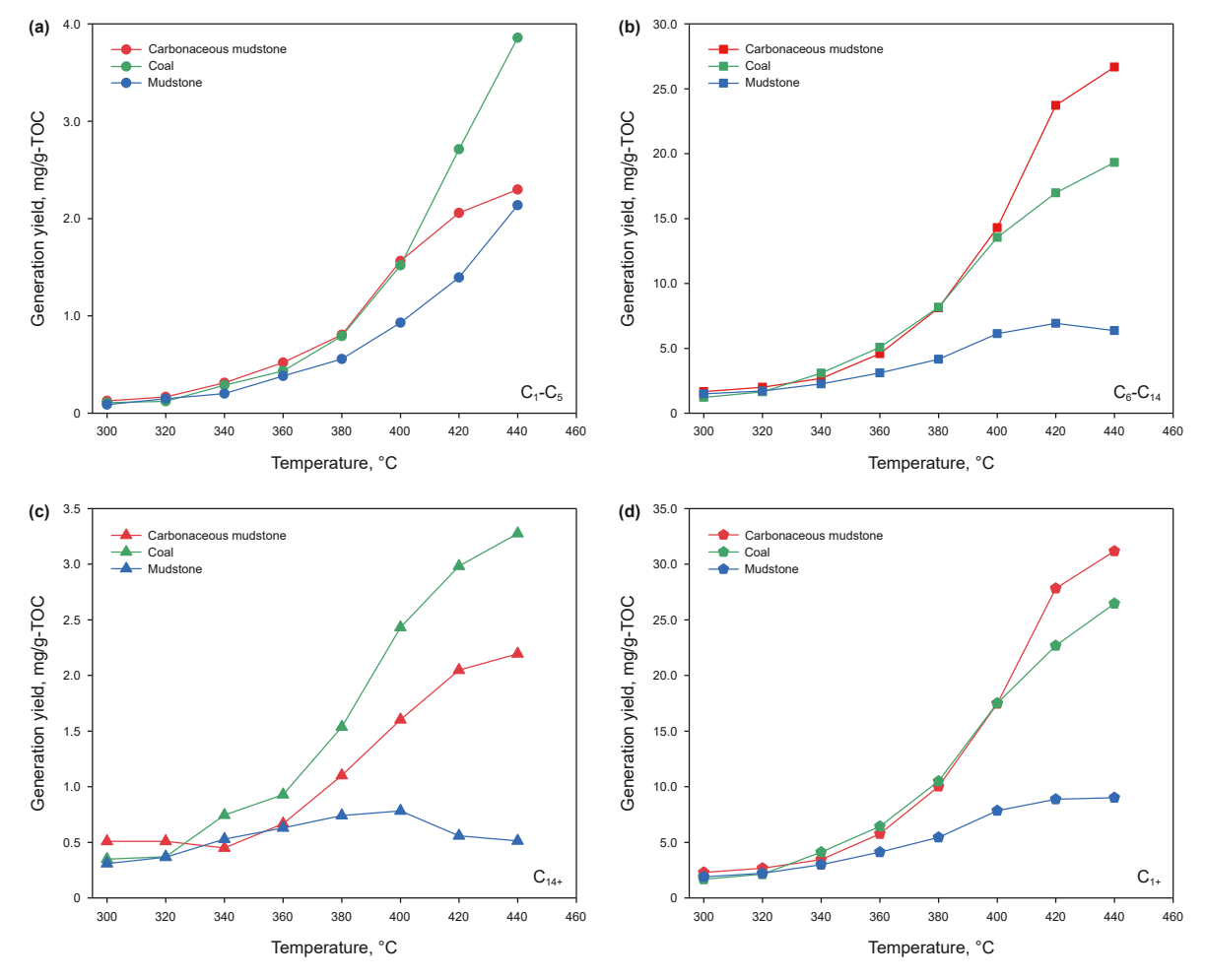


Fig. 18. Yields of (a) gaseous hydrocarbons, (b) light hydrocarbons, (c) heavy hydrocarbons, and (d) total produced hydrocarbons from pyrolysis experiments in semi-open systems.

#### 5. Conclusion

In this study, FTIR tests and semi-open thermal simulation experiments were conducted on Jurassic coal-measure source rocks from the Junggar Basin. The following conclusions were drawn.

- (1) Among the three types of source rocks, coal has a higher percentage of aromatic structures but a lower percentage of carbon atoms as well as the lowest DOC; it also has a higher degree of branched chaining in aliphatic structures than carbonaceous mudstones and is relatively rich in C–H structures of aliphatic structures. Mudstone has opposite characteristics to coals.
- (2) The molecular structure of coal–measure source rocks is closely related to their hydrocarbon potential. The aromatic structure parameters  $f_a$ , I, and DOC are negatively correlated with the organic matter abundance parameters and are better correlated with TOC. For the aliphatic structure parameters, H is positively correlated with  $S_1+S_2$  values, and A is correlated with the organic matter type. The better the organic matter type, the larger the A value.
- (3) The characteristics of organic molecular structure efficiently explain the results of the semi-open thermal simulation experiment: The degree of aliphatic hydrogen enrichment of carbonaceous mudstone is similar to that of coal, but the relative abundance of the aliphatic group of carbonaceous mudstone is higher and the *DOC* of aromatic structure is

lower, which makes the hydrocarbon generation base stronger and easier to crack. Among the types of source rocks, coal has the highest degree of branched chaining in the aliphatic structure, corresponding to the highest gaseous hydrocarbon yield. However, mudstone has the lowest hydrocarbon generation yield as it also has the lowest aliphatic abundance and hydrogen enrichment and the highest degree of aromatic structure condensation.

#### **Declaration of competing interest**

The authors declare that they have no known competing financial interests or personal relationships that could have appeared to influence the work reported in this paper.

## **CRediT authorship contribution statement**

**Tian-Chen Ge:** Writing — review & editing, Writing — original draft, Methodology, Formal analysis, Data curation, Conceptualization. **Xiang-Chun Chang:** Project administration, Methodology, Investigation, Conceptualization. **Guan-Long Zhang:** Resources, Project administration, Methodology, Data curation. **Jun-Jian Zhang:** Writing — review & editing, Methodology, Investigation, Conceptualization. **Rui-Chao Guo:** Software, Resources, Methodology, Investigation. **Wei-Zheng Gao:** Software, Investigation, Formal analysis. **Ling-Yu Zhao:** Software, Resources. **Shang-Bin** 

**Wang:** Software, Methodology, Formal analysis. **Jia-Qi Duan:** Software, Methodology.

#### Acknowledgments

This study was co-funded by the National Natural Science Foundation of China (Grant Nos. 42372160, 42072172), Shandong Province Natural Science Fund for Distinguished Young Scholars (Grant No. JQ201311), and the Graduate Scientific and Technological Innovation Project financially supported by Shandong University of Science and Technology (Grant No. SDKDYC190313). We thank the Shengli Oil Company of Sinopec for approving the publication.

#### References

- Adams, M.J., Awaja, F., Bhargava, S., et al., 2005. Prediction of oil yield from oil shale minerals using diffuse reflectance infrared Fourier transform spectroscopy. Fuel 84 (14–15), 1986–1991. https://doi.org/10.1016/j.fuel.2005.04.011.
- Bayon, R.L., Brey, G.P., Ernst, W.G., et al., 2011. Experimental kinetic study of organic matter maturation: time and pressure effects on vitrinite reflectance at 400 °C. Org. Geochem. 42 (4), 340–355. https://doi.org/10.1016/ j.orggeochem.2011.01.011.
- Cao, J., Wang, X.L., Sun, P.A., et al., 2012. Geochemistry and origins of natural gases in the central Junggar Basin, Northwest China. Org. Geochem. 53, 166–176. https://doi.org/10.1016/j.orggeochem.2012.06.009.
- Cesar, J., Quintero, K., 2020. Organic geochemistry of kerogen from La Luna Formation, Western Venezuelan Basin, using diffuse reflectance–Fourier transform infrared spectroscopy (DRFTIR). Fuel 282, 118805. https://doi.org/10.1016/j.fuel.2020.118805.
- Chen, J.P., Zhao, C.Y., He, Z.H., 1997. Criteria for evaluation the hydrocarbon generating potential of organic matter in coal measure. Petrol. Explor. Dev. 24 (1), 1–5, 91. (in Chinese).
- Chen, Y.Y., Furmann, A., Mastalerz, M., et al., 2014. Quantitative analysis of shales by KBr-FTIR and micro-FTIR. Fuel 116, 538–549. https://doi.org/10.1016/j.fuel.2013.08.052.
- Cornford, C., Gardner, P., Burgess, C., 1998. Geochemical truths in large data sets. I: Geochemical screening data. Org. Geochem. 29 (1–3), 519–530. https://doi.org/10.1016/S0146-6380(98)00189-2.
- Curry, D.J., Emmett, J.K., Hunt, J.W., 1994. Geochemistry of aliphatic-rich coals in the Cooper Basin, Australia and Taranaki basin, New Zealand: implications for the occurrence of potentially oil-generative coals. In: Scott, A.C., Fleet, A.J. (Eds.), Coal and Coal-bearing Strata as Oil-prone Source Rocks?, vol. 77. Geological Society Special Publication, pp. 149–182.
- Ding, W.C., Li, T.D., Chen, X.H., et al., 2020. Intra-continental deformation and tectonic evolution of the West Junggar Orogenic Belt, Central Asia: Evidence from remote sensing and structural geological analyses. Geosci. Front. 11 (2), 651–663. https://doi.org/10.1016/j.gsf.2019.08.001.
- Gan, H.J., Wang, H., Chen, J., et al., 2018. Geochemical characteristics of Jurassic coal and its paleoenvironmental implication in the eastern Junggar Basin, China. J. Geochem. Explor. 188, 73–86. https://doi.org/10.1016/j.gexplo.2018.01.010.
- Gong, D.Y., Wang, Y., Yuan, M., et al., 2017. Genetic types and origins of natural gases from eastern Fukang sub-depression of the Junggar Basin, NW China: implication for low-mature coal-derived gases. Journal of Natural Gas Geoscience 2 (3), 179–189. https://doi.org/10.1016/j.jnggs.2017.07.002.
- Guo, J.H., Zhou, Y.R., Yan, Y.H., et al., 2014. Evolutional characteristics of the kerogen molecular structure during the low-mature stage: An infrared spectra analysis. Geochimica 43 (5), 529–537 (in Chinese).
   Guo, X.B., Shi, B.H., Li, Y., et al., 2022. Closed-system pyrolysis-based hydrocarbon
- Guo, X.B., Shi, B.H., Li, Y., et al., 2022. Closed-system pyrolysis-based hydrocarbon generation simulation and gas potential evaluation of the Shanxi Formation shales from the Ordos Basin, China. Energy Geoscience 3 (1), 8–16. https:// doi.org/10.1016/j.engeos.2021.09.001.
- Han, W.X., Luo, X., Lin, S.H., et al., 2023. Geochemical parameters of thermal simulation of gas generation on lacustrine Type II shales in semi-open pyrolysis system. Geoenergy Science and Engineering. https://doi.org/10.1016/ j.geoen.2023.212178.
- He, X.Q., Liu, X.F., Nie, B.S., et al., 2017. FTIR and Raman spectroscopy characterization of functional groups in various rank coals. Fuel 206, 555–563. https:// doi.org/10.1016/j.fuel.2017.05.101.
- Hou, L.H., Ma, W.J., Luo, X., et al., 2021a. Hydrocarbon generation–retention–expulsion mechanism and shale oil producibility of the Permian lucaogou shale in the Junggar Basin as simulated by semi-open pyrolysis experiments. Mar. Petrol. Geol. 125, 104880. https://doi.org/10.1016/j.marpetgeo.2020.104880.
- Hou, M.G., Zha, M., Ding, X.J., et al., 2021b. Source and accumulation process of jurassic biodegraded oil in the eastern Junggar Basin, NW China. Petrol. Sci. 18 (4), 1033–1046. https://doi.org/10.1016/j.petsci.2021.07.010.
- Huang, H.P., Li, M.H., Yang, C., et al., 2023. A comparison of hydrocarbon generation and expulsion in carbonate and argillaceous source rocks using semi-open pyrolysis experiments. Mar. Petrol. Geol. 155, 106382. https://doi.org/10.1016/ i.marpetgeo.2023.106382.
- Ibarra, J.V., Munoz, E., Moliner, R., et al., 1996. FTIR study of the evolution of coal

- structure during the coalification process. Org. Geochem. 24 (6-7), 725–735. https://doi.org/10.1016/0146-6380(96)00063-0.
- Isaksen, G.H., Curry, D.J., Yeakel, J.D., Jenssen, A.L., 1998. Controls on the oil and gas potential of humic coals. Org. Geochem. 29, 22–44. https://doi.org/10.1016/ S0146-6380(98)00042-4.
- Killops, S.D., Funnell, R.H., Suggate, R.P., et al., 1998. Predicting generation and expulsion of paraffinic oil from vitrinite-rich coals. Org. Geochem. 29, 1–21. https://doi.org/10.1016/S0146-6380(98)00087-4.
- Li, J., Jiang, Z.L., Luo, X., et al., 2009. Geochemical characteristics of coal–measure source rocks and coal–derived gas in Junggar basin, NW China. Petrol. Explor. Dev. 36 (3), 365–374. https://doi.org/10.1016/S1876-3804(09)60133-6.
- Li, X., Fu, X.H., Liu, A.H., et al., 2016. Methane adsorption characteristics and adsorbed gas content of low-rank coal in China. Energy Fuel. 30 (5), 3840–3848. https://doi.org/10.1021/acs.energyfuels.6b00071.
- Li, X., Fu, X.H., Yang, X.S., et al., 2018. Coalbed methane accumulation and dissipation patterns: a case study of the Junggar basin, NW China. J. Asian Earth Sci. 160, 13–26. https://doi.org/10.1016/j.jseaes.2018.04.003.
  Li, J., Hao, A.S., Qi, X.N., et al., 2019. Geochemical characteristics and exploration
- Li, J., Hao, A.S., Qi, X.N., et al., 2019. Geochemical characteristics and exploration potential of Jurassic coal–formed gas in northwest China. Journal of Natural Gas Geoscience 4 (6), 321–335. https://doi.org/10.11764/j.issn.1672-1926.2019.05.018.
- Lis, G.P., Mastalerz, M., Schimmelmann, A., et al., 2005. FTIR absorption indices for thermal maturity in comparison with vitrinite reflectance R<sub>o</sub> in type-II kerogens from Devonian black shales. Org. Geochem. 36 (11), 1533–1552. https://doi.org/10.1016/j.orggeochem.2005.07.001.
- Liu, X., He, X., 2017. Effect of pore characteristics on coalbed methane adsorption in middle-high rank coals. Adsorption 23 (1), 3–12. https://doi.org/10.1007/ s10450-016-9811-z.
- Liu, Y., Zhu, Y.M., Li, W., et al., 2016. Molecular simulation of methane adsorption in shale based on grand canonical Monte Carlo method and pore size distribution.

  J. Nat. Gas Sci. Eng. 30, 119–126. https://doi.org/10.1016/j.jngse.2016.01.046.
- Long, J., Zhang, S.X., Luo, K.L., 2023. Discovery of anomalous gallium enriched in stone coal: Significance, provenance and recommendations. Geosci. Front. 14 (4), 101538. https://doi.org/10.1016/j.gsf.2023.101538.
- Marshall, C.P., Wilson, M.A., Hartung-Kagi, B., et al., 2001. Potential of emission Fourier transform infrared spectroscopy for in situ evaluation of kerogen in source rocks during pyrolysis. Chem. Geol. 175 (3-4), 623–633. https://doi.org/ 10.1016/S0009-2541(00)00383-1.
- Painter, P.C., Snyder, R.W., Starsinic, M., et al., 1981. Concerning the application of FT–IR to the study of coal; a critical assessment of band assignments and the application of spectral analysis programs. Appl. Spectrosc. 35 (5), 475–485. https://doi.org/10.1366/0003702814732256.
- Pan, Y.H., Li, M.W., Sun, Y.G., et al., 2023. Characterization of free and bound bitumen fractions in a thermal maturation shale sequence. Part 2: Structural evolution of kerogen and bitumen during shale oil generation, expulsion and retention. Org. Geochem. 182, 104640. https://doi.org/10.1016/ j.orggeochem.2023.104640.
- Patterson, J.H., Ramsden, A.R., Dale, L.S., et al., 1986. Geochemistry and mineralogical residences of trace elements in oil shales from Julia Creek, Queensland, Australia. Chem. Geol. 55 (1–2), 1–16. https://doi.org/10.1016/0009-2541(86) 90123-3.
- Peters, K.E., 1986. Guidelines for evaluating petroleum source rock using programmed pyrolysis. Am. Assoc. Petrol. Geol. Bull. 70 (3), 318–329. https://doi.org/10.1306/94885688-1704-11D7-8645000102C1865D.
- Powell, T.G., Boreham, C.J., 1991. Petroleum generation and source rock assessment in terrigenous sequences. APEA J. 31 (2), 297–311.
- Qiao, J.Q., Liu, L.F., Shang, X.Q., 2020. Deposition conditions of the jurassic lacustrine source rocks in the east fukang Sag, Junggar Basin, NW China: Evidence from major and trace elements. Geol. J. 55 (7), 4936–4953. https://doi.org/10.1002/ gi.3714.
- Qiu, Z.K., He, N.X., Wang, H., et al., 2021. The sedimentological reservoir characteristics of the jurassic Sangonghe formation, southern mahu slope, Junggar Basin, northwestern China. Geol. J. 56 (3), 1478—1495. https://doi.org/10.1002/gi4014
- Takahashi, K.U., Suzuki, N., 2017. Semi-open and closed system pyrolysis of Paleogene coal for evaluating the timing of hydrocarbon gas expulsion. Int. J. Coal Geol. 178, 100–109. https://doi.org/10.1016/j.coal.2017.05.004.
- Tao, S., Chen, S.D., Tang, D.Z., et al., 2018. Material composition, pore structure and adsorption capacity of low-rank coals around the first coalification jump: a case of eastern Junggar basin, China. Fuel 211, 804–815. https://doi.org/10.1016/ i.fuel.2017.09.087.
- Wang, S.Q., Tang, Y.G., Schobert, H.H., et al., 2011. FTIR and <sup>13</sup>C NMR investigation of coal component of late permian coals from Southern China. Energy Fuel. 25 (12), 5672–5677. https://doi.org/10.1021/ef201196v.
- Wang, Q., Ye, J.B., Yang, H.Y., et al., 2016. Chemical composition and structural characteristics of oil shales and their kerogens using Fourier transform infrared (FTIR) spectroscopy and solid-state <sup>13</sup>C nuclear magnetic resonance (NMR). Energy Fuel. 30 (8), 6271–6280. https://doi.org/10.1021/acs.energyfuels.6b00770.
- Wang, T., Deng, Z., Hu, H.Y., et al., 2021. Potential analysis of Jurassic coal-bed gas resources in Tuha basin. China Sciencepaper 16 (9), 1023–1034 (in Chinese).
- Wang, Q.C., Chen, D.X., Gao, X.Z., et al., 2023. Overpressure origins and evolution in deep-buried strata: A case study of the Jurassic Formation, central Junggar Basin, western China. Petrol. Sci. 20 (3), 1429–1445. https://doi.org/10.1016/j.petsci.2022.12.015.

- Wu, C.J., Zhang, M.F., Xiong, D.M., et al., 2020. Gas generation from Jurassic coal measures at low mature stage and potential gas accumulation in the eastern Junggar Basin, China. J. Nat. Gas Sci. Eng. 84, 103692. https://doi.org/10.1016/ i.ingse.2020.103692.
- Yang, H., Gong, W.P., Zheng, L.J., 2021. Characteristics of oil and gas generation expelling and retention of coaly source rock, Petrol. Geol. Exp. 43 (3), 498–506 (in Chinese).
- Yang, R.Y., Li, G.S., Qin, X.Z., et al., 2022. Productivity enhancement in multilayered coalbed methane reservoirs by radial borehole fracturing. Petrol. Sci. 19 (6), 2844–2866. https://doi.org/10.1016/j.petsci.2022.06.019.
- Yao, Z.Q., Yang, F., Jianatayi, D., et al., 2022. Application of multi-attribute matching technology based on geological models for sedimentary facies: A case study of the 3rd member in the Lower Jurassic Badaowan Formation, Hongshanzui area, Junggar Basin, China. Petrol. Sci. 19 (1), 116–127. https://doi.org/10.1016/ i.petsci.2021.10.008.
- Yu, M., Gao, G., Jin, J., et al., 2022. Hydrocarbon generation simulation of coaly source rocks in the Lower combination on the southern margin of Junggar Basin and indications for oil and gas sources of well Gaotan 1. Petrol. Geol. Exp. 44 (4), 687–697 (in Chinese)
- Zeng, L.F., 2020. Petroleum Generation Kinetics of Jurassic Coaly Source Rocks in Junggar Basin. Doctoral degree thesis, University of Chinese Academy of Sciences (in Chinese).
- Zhang, Y.J., Liu, G.D., 2002. Characteristics and evolution of composite petroleum systems and the exploration strategy in Junggar Basin northwest China. Petrol. Explor. Dev. 29 (1) 36–39 (in Chinese)
- Explor. Dev. 29 (1), 36–39 (in Chinese).

  Zhang, G.L., Wang, Y., 2023. Tectono-sedimentary framework of early permian in Junggar Basin and its petroleum geological significance. Petrol. Geol. Recov.

- Effic. 30 (1), 35-48 (in Chinese).
- Zhang, J.J., Wei, C.T., Zhao, C.J., et al., 2021. Effects of nano-pore and macromolecule structure of coal samples on energy parameters variation during methane adsorption under different temperature and pressure. Fuel 289, 119804. https://doi.org/10.1016/j.fuel.2020.119804.
- Zhang, H.H., Zhang, Z.C., Tang, W.H., et al., 2022. Burial and exhumation history of Jurassic sedimentary rocks in the southern margin of the Junggar Basin: implications for the growth of the northern Tianshan Mountains. J. Asian Earth Sci. 236, 105339. https://doi.org/10.1016/j.jseaes.2022.105339.
- Zhi, D.M., Zhang, J.K., Wu, T., et al., 2023. Yanshanian-Himalayan geodynamic transformation of the northwestern Junggar Basin, southwestern Central Asian Orogenic Belt (CAOB), and its significance for petroleum accumulation. Geosci. Front. 14 (4), 101565. https://doi.org/10.1016/j.gsf.2023.101565.
- Zhou, F.B., Liu, S.Q., Pang, Y.Q., et al., 2015. Effects of coal functional groups on adsorption microheat of coal bed methane. Energy Fuel. 29 (3), 1550–1557. https://doi.org/10.1021/ef502718s.
- Zhu, M., Liang, Z.L., Wang, X., et al., 2023a. Mesozoic strike-slip fault system at the margin of the Junggar Basin, NW China. J. Struct. Geol. 175, 104950. https://doi.org/10.1016/j.jsg.2023.104950.
- Zhu, Z.J., Li, Q., Chen, H.H., et al., 2023b. Tectonic-geomorphological evolution and provenance-sedimentary response: Insights from the middle jurassic-lower cretaceous, Junggar Basin, China. Mar. Petrol. Geol. 158, 106514. https://doi.org/10.1016/j.marpetgeo.2023.106514.
- Zhu, X.S., Huang, Y.S., Wang, T., et al., 2023c. Crustal structures inferred from bouguer gravity anomalies in the altai orogen, Junggar Basin, tianshan orogen, and tarim basin. J. Asian Earth Sci. 257, 105842. https://doi.org/10.1016/ j.jseaes.2023.105842.